Journal of Materials Science Research and Reviews

Volume 7, Issue 2, Page 315-338, 2024; Article no.JMSRR.119667

Titanium Dioxide One-Dimensional Nanostructures as Photoanodes for Dye-Sensitized Solar Cells

Simon Bbumba [a,b]*, Ibrahim Karume [a], Moses Kigozi [c], Hussein Kisiki Nsamba [a], Collins Letibo Yikii [a], Resty Alexandra Nazziwa [a], Ivan Kiganda [a] and Muhammad Ntale [a]

[a] *Department of Chemistry, College of Natural Sciences, Makerere University, P.O. Box 7062, Kampala, Uganda.*
[b] *Department of Science, Faculty of Science and Computing, Ndejje University, P.O. Box 7088, Kampala, Uganda.*
[c] *Department of Chemistry, Busitema University, P.O. Box 236, Tororo, Uganda.*

Authors' contributions

This work was carried out in collaboration among all authors. All authors read and approved the final manuscript.

Article Information

Open Peer Review History:
This journal follows the Advanced Open Peer Review policy. Identity of the Reviewers, Editor(s) and additional Reviewers, peer review comments, different versions of the manuscript, comments of the editors, etc are available here: https://www.sdiarticle5.com/review-history/119667

Review Article

Received: 01/05/2024
Accepted: 05/07/2024
Published: 09/07/2024

ABSTRACT

Herein, we reviewed the titanium dioxide one-dimensional nanostructures which are commonly applied as photoanodes for dye-sensitized solar cells (DSSCs). Titanium dioxide is the commonly used semiconductor electrode due to its low toxicity, mechanical stability, and availability during DSSCs application. The efficiency of the DSSCs having a titanium dioxide photoanode is mainly

---

**Corresponding author: Email: sbbumba@ndejjeuniversity.ac.ug;*

Cite as: *Bbumba, Simon, Ibrahim Karume, Moses Kigozi, Hussein Kisiki Nsamba, Collins Letibo Yikii, Resty Alexandra Nazziwa, Ivan Kiganda, and Muhammad Ntale. 2024. "Titanium Dioxide One-Dimensional Nanostructures As Photoanodes for Dye-Sensitized Solar Cells". Journal of Materials Science Research and Reviews 7 (2):315-38. https://journaljmsrr.com/index.php/JMSRR/article/view/334.*

determined by the changes in the short circuit current (J_{sc}). The TiO_2 nanoparticles have shown an efficiency of 12 % which is the highest. Other nanostructures such as nanotubes (11.05 %), nanowires (8.90 %), and nanofibers (8.0 %) have also been used as anodes. The TiO_2 nanostructures have a high surface area that enhances dye loading but also increases the short circuit current hence leading to a high conversion efficiency. This review also introduces the commonly used characterization techniques for titanium dioxide one-dimensional nanostructures which explain crystal orientation, morphology, surface functional groups, surface area, elemental composition, and other chemical properties.

Keywords: titanium dioxide; short circuit current; photoanode; nanotubes; nanowires; efficiency.

1. INTRODUCTION

In recent years the use of fossil fuels as a source of energy has seen a rapid increase due to several human activities such as mining, industrialization, and farming. These fuels which include coal and petroleum give off greenhouse gases that pollute air, land, and water thus endangering humans and aquatic life [1]. Utilization of solar energy as an alternative renewable energy source is an efficient and modest way however the irradiation that reaches the earth is significantly higher than the human energy demand [2]. It has been determined that the amount of solar radiation that reaches the Earth is 3.8 million EJ/year [3]. Research is currently ongoing to develop efficient solar energy capture, conversion, and cheap storage technologies, simple in design and non-toxic [4,5, 5a]. In 1972 Honda and Fujishima used the photoelectric effect to explain the application of TiO_2 in oxidation and reduction after its photo-induction [6]. Photo voltaic devices which use the photoelectric effect to convert solar energy to electricity have seen rapid growth since they do not emit greenhouse gases or any other toxic substances [7]. Over the years different solar-to-electricity conversion devices have been fabricated with varying efficiencies as shown in Fig. 1.

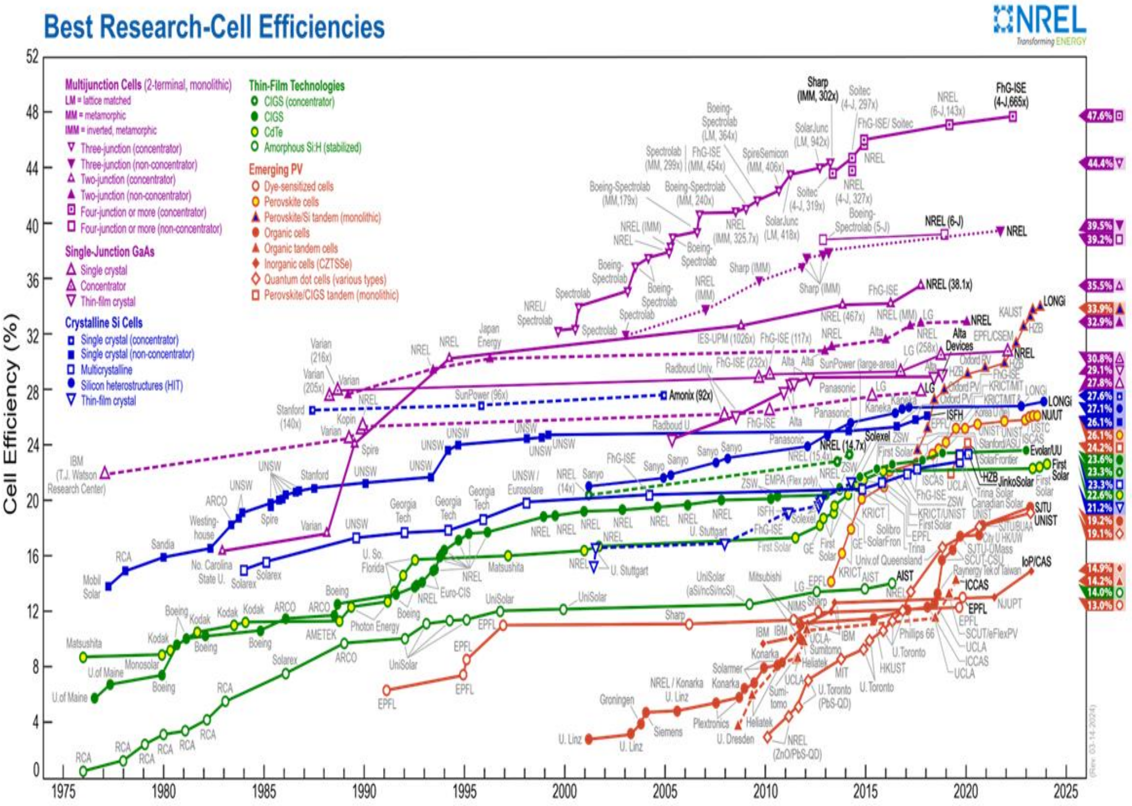

Fig. 1. Various solar-electricity conversion technologies over a range of years (1975-2025)

The conventional first-generation silicon-based solar cells which have complicated fabrication techniques and high costs limit their commercialization in domestic applications [8]. This was solved by Michael Grätzel and Brian O'Regan in 1991 when they demonstrated dye-sensitized solar cells (DSSCs) that could give efficiencies in the range of 7.1-7.9 % using a TiO_2 nanostructure photoanode coated with ruthenium dye [9]. The dye-sensitized solar cell has five components which include the photoanode [10], dye sensitizer [11], counter electrode [12], conductive substrate [13] and the electrolyte (redox couple) [14]. The dye sensitizer functions to absorb a photon of energy which then causes photo excitation of an electron to the conduction band of the semiconductor. The photoanode acts as an anchor onto which the photosensitizer is attached but also transports the electron to the load. The counter electrode plays the role of returning the electron back to the circuit to regenerate the redox couple. The redox couple regenerates the oxidized dye to its normal state. The photoanode whose function is to collect and transport the electrons to the external circuit is of great importance in the DSSCs [15]. Semiconductor materials are mainly up of TiO_2 [16], SnO_2 [17], Fe_2O_3 [18] and ZnO [19,20] which have found wide application as anode electrodes in DSSCs. The nanostructured TiO_2 materials have found application as semiconductor materials due to their large surface area which improves dye loading and the overall efficiency of the cell. The commonly used semiconductor nanostructures include nanowires, nanoparticles, nanotubes, nanoflowers, nanoribbons, nano-onions, nanoflakes, and nanofibers. Titanium dioxide nanoparticles having ruthenium as the dye sensitizer have conversion efficiencies of 12 % in the lab and 32 % theoretically [21,22]. The light scattering drawbacks and low conversion efficiencies faced by TiO_2 nanostructures can be solved through doping which improves the efficiency. Several cations such as Tungsten (W) [23], Nickel (Ni) [24], Niobium (Nb) [25] and Lanthanum (La) [26] have been used as dopants to improve electron mobility and light absorption. Also, non-metals such as Fluorine (F) [27], Carbon (C) [28], Nitrogen (N) [29,30] and Sulphur (S) [31] have also been applied to modify the electronic properties of TiO_2. This review aims to illustrate the Titanium dioxide photoanode one-dimensional nanostructures and how they influence the dye-sensitized solar cell performance. Furthermore, different photoanode characterization techniques are discussed as well as the overall performance of the nanowires, nanoparticles, nanotubes, and nanofibers [30a].

2. WORKING PRINCIPLE AND PHOTOCHEMICAL CHARACTERIZATION TECHNIQUES OF DSSCS

The dye-sensitized solar cell consists of five components which include the semiconductor, electrolyte with its redox couple, dye sensitizer, counter electrode, and transparent conductive oxide as shown in Fig. 2.

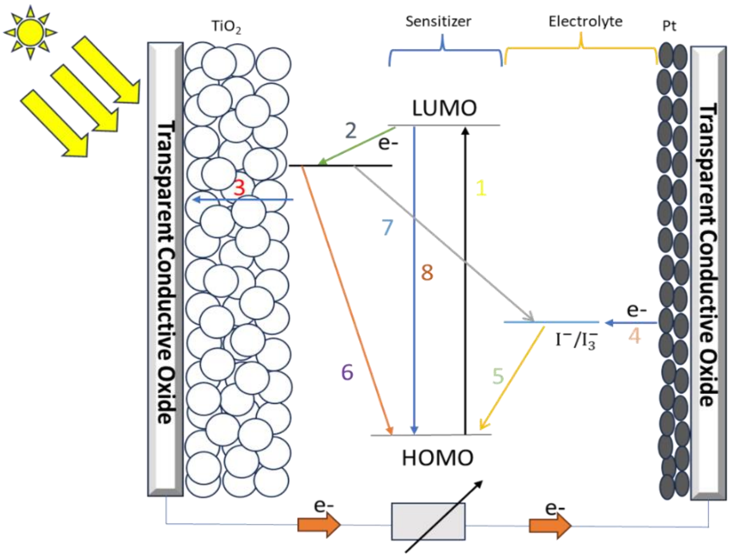

Fig. 2. Electron transfer in the various dye-sensitized solar cell components

The dye sensitizer plays the role of absorbing a photon of energy which generates an electron through excitation from the highest occupied molecular orbital (HOMO) to the lowest unoccupied molecular orbital (LUMO) which leads to injection of the charges to the conduction band of the metal oxide. The semiconductor which is usually made of TiO_2 serves the function of acting as an anchor onto which the load gets attached through its large surface area but also a wide band gap for light harvesting. In addition, the transparent conductive which is either made of Flourine or Indium acts as a support for the semiconductor but also to transport the electrons to the external load. Furthermore, the electrolyte mainly containing iodide/triiodide redox couple acts as an electrical medium between the counter electrode and the working electrode but also in the regeneration of the oxidized dye sensitizer molecule. Lastly, the counter electrode plays an important role in returning the electron to the circuit but also acts as an electrocatalyst for better photovoltaic performance.

The characterization of the photovoltaic performance of the dye-sensitized solar cells is mainly carried out using three main techniques that are Photocurrent – voltage (I-V) measurements, Electrochemical Impedance Spectroscopy (EIS), and Incident to photon current conversion efficiency (IPCE).

Photocurrent–voltage (I-V) measurements are used to determine the electrical output power at 1.5 standard global air Mass (AM) and solar radiation of 1000 W/m^2 occurring at a temperature of 25 °C [32]. It gives four parameters which include the open circuit voltage (V_{oc}), short circuit current (J_{sc}), fill factor (FF), and power conversion efficiency (PCE, η) as shown in Fig. 3 [33].

The open circuit voltage (V_{oc}) is defined as the maximum voltage to the external load which is a result of the electron quasi-fermi level and the electron separation hole [34]. It gives information on the difference between the electrochemical potential of the redox couple and the fermi level of the photoanode. V_{oc} is measured at open circuit conditions for which the current that flows is zero (I = 0). The short circuit current (J_{sc}) is measured as the maximum current output of the solar cell. J_{sc} is measured at short circuit conditions for which the potential applied is zero (V=0) and is influenced by several factors such as the electrochemical properties of the photoanode when in contact with the electrolyte solution, molecular structure of the dye sensitizer, and amount of dye adsorbed on the photo anode [35]. J_{sc} is a result of the proportionality of the diffusion length and is defined as shown in (Equation 1).

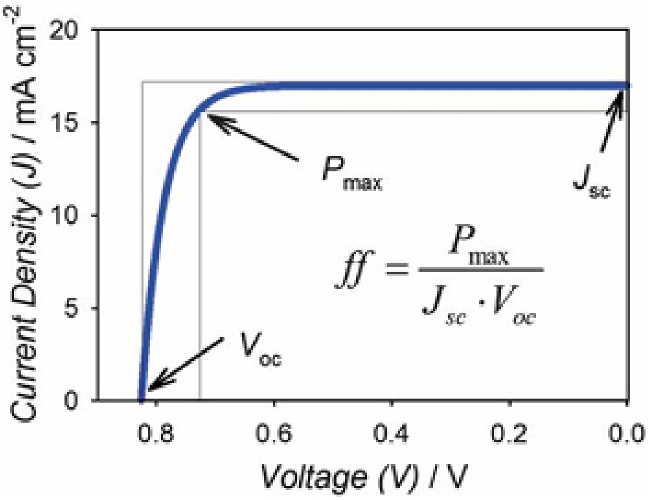

Fig. 3. I-V curve showing the different photochemical parameters. Reprinted with permission ref [33]. Copyright 2011, The Royal Society of Chemistry

$$J_{sc} = qG(L_n + L_p) \qquad (1)$$

In addition, the fill factor gives information regarding the ideality of the solar cell which in brief is the ratio of the maximum power (P_{max}) to the product of V_{oc} and J_{sc} (Equation 2) and varies in the range of 0-1 which values influence the rectangular shape of the graph.

$$FF = \frac{P_{max}}{V_{oc} \times J_{sc}} = \frac{V_{max} J_{max}}{V_{oc} \times J_{sc}} \qquad (2)$$

Lastly, the power conversion efficiency of a solar cell is the ratio of the maximum power (P_{max}) to the incident power (P_{in}) under illumination of 1.5 standard global Air Mass (AM). The increased overall power conversion efficiency of the cell is greatly influenced by high values of V_{oc}, J_{sc}, and FF as shown in (Equation 3).

$$\eta = \frac{P_{max}}{P_{in}} = \frac{V_{oc} \times J_{sc} \times FF}{P_{in}} \qquad (3)$$

In addition, Electrochemical Impedance Spectroscopy which is a dynamic technique gives information regarding the kinetics of charge and photochemical reactions in the DSSCs [36,37]. The EIS, once a potential is applied, generates a small sine wave that influences the sinusoidal current output and sinusoidal alternating potential which are plotted against variations in frequency modulation but represented in phase shift and amplitude [38]. The ratio of current to voltage in the frequency domain is measured in both real and imaginary parts which defines the impedance (Z). It is observed that the impedance of a resistor is independent of frequency and has both real (Z´) and imaginary (Z˝) parts while the capacitor and inductor form variation with frequency and only have imaginary parts. The impedance is determined at various frequencies (ω) by schematic representations of Nyquist plots (Z´Vs Z˝) and Bode plot **|**Z**|** vs (ω), Ø is the phase of Z (ω) [39]. The Nyquist plot of impedance spectrum as used in DSSCs contains three semicircles which are fitted by a transmission line equivalent circuit (TLC) as shown in Fig. 4 [40].

The high-frequency semicircle is a result of Helmholtz capacitance of the counter electrode and charge transfer resistance while the middle-frequency semicircle shows the capacitance of the photoanode and recombination resistance at the photoanode/electrolyte interface and the low-frequency semicircles describe the impedance diffusion in the electrolyte (Warburg element, W_s) [41,42]. During DSSCs measured using EIS, an electrical observation is made that the cell module consists of capacitors and resistors. EIS measurements are used to identify the capacitance and resistance in the different DSSCs components that is redox couple diffusion in the electrolyte, capacitance of the mesoporous metal oxide, charge transfer resistance of the counter electrode, recombination resistance at the interfaces of the semiconductor/dye/electrolyte and series resistance due to sheet resistance of TCO at the contact resistance [43–46].

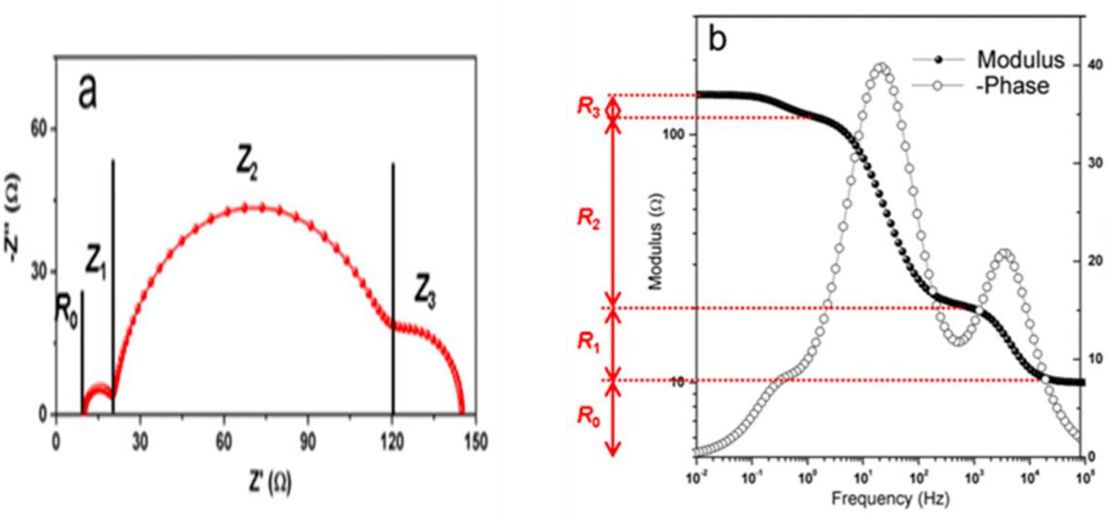

Fig. 4. A schematic representation of Nyquist (a) and Bode (b) Plots. Reprinted with permission ref [40]. Copyright 2017, Elsevier

Lastly, Incident to photon current conversion efficiency (IPCE) is the ratio of the photo-generated electrons ($N_{electrons}$) flowing through the external circuit to the incident photons ($N_{photons}$) at a given wavelength which is described in (Equation 4).

$$\text{IPCE } (\lambda) = \frac{N_{\text{electrons}}\,(\lambda)}{N_{\text{photons}}\,(\lambda)} \tag{4}$$

This measurement gives information regarding how much the DSSCs convert incident photons to electrons at a given wavelength. A high IPCE value corresponds to increased DSSCs conversion efficiencies of the photons to electrons hence a better yield. This can further be evaluated using (Equation 5) [47–49].

$$\text{IPCE } (\lambda) = \text{LHE}(\lambda)\ \eta_{inj}(\lambda)\ \eta_{col}(\lambda) \tag{5}$$

Where LHE, the light-harvesting efficiency, η_{inj} is the quantum yield of the electron injection and η_{col} is the charge collection efficiency.

Using IPCE measurement the mesoporous photo anode has better efficiency due to its ability to highly collect charge carriers and favorable photodegradation.

3. CHARACTERIZATION TECHNIQUES OF PHOTOANODES IN DSSCS

The methods that are used to understand the crystal orientation, morphology, surface functional groups, surface area, elemental composition, and other physical and chemical properties of the nanomaterials are termed Characterization techniques [50]. The commonly used characterization techniques include X-ray Diffraction (XRD) [51], Scanning Electron Microscopy (SEM), X-ray Photoelectron Spectroscopy (XPS) [52], Transmission Electron Spectroscopy (TEM) [53], Scanning Transmission Electron microscopy (STEM) [54], Raman Spectroscopy [55], Thermogravimetric Analysis (TGA) [56], UV-visible Spectroscopy [57], Brunauer-Emmett-Teller (BET) [58] and Fourier Transform Infrared Spectroscopy (FTIR) [59].

Scanning Electron Microscopy (SEM) is a characterization technique that is used to determine the morphology and composition of a given material. A high-energy electron beam is used to scan the nanomaterials and the magnified image is formed through mapping signal intensity and scan rate [60,61]. Yao et al [62] carried out SEM analysis on Carbon nanofibers-TiO_2 nanoparticles to analyze the morphology as shown in Fig. 5.

The carbon nanofibers with a diameter of 600 nm are observed to have a smooth surface which is revealed in Figure (a). Figure (b) shows the morphology of TiO_2 nanoparticles-carbon nanofibers which TiO_2 forms clusters on the surface which makes it rough but also theirs a reduction in the diameter (300 nm) of the TiO_2 nanoparticles-carbon nanofibers composite.

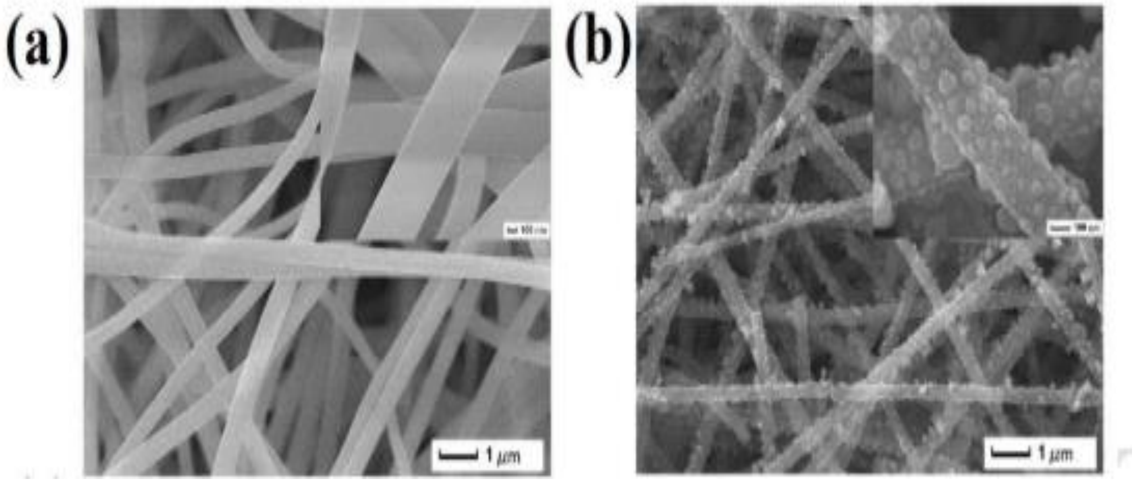

Fig. 5. SEM image (a) carbon nanofibers and (b) TiO_2 nanoparticles-carbon nanofibers. Reprinted with permission ref [62]. Copyright 2019, Elsevier

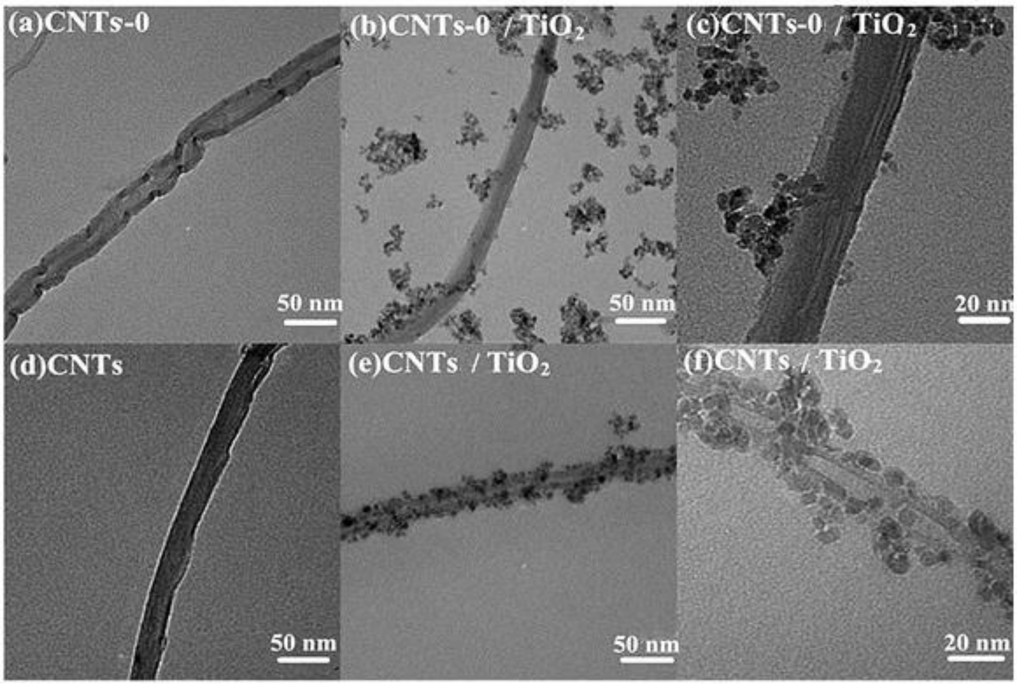

Fig. 6. TEM image of titanium dioxide particles and carbon nanotubes. reprinted with permission ref [63]. Copyright 2020, Elsevier

Transmission Electron microscopy (TEM) is a technique used to understand the inside of a material with great detail due to its high resolution and ability to even show small interactions between nanoparticles and their constituents. It has a small wavelength hence able to produce images in the sub-nanometer resolution with enough energy that can easily penetrate even very small crystals. Li et al. [63] used TEM analysis (Fig. 6) to determine the interaction and compatibility of TiO_2 nanoparticles and carbon nanotubes.

The TiO_2 nanoparticle (5-10 nm) agglomerate to form clusters and are uniformly distributed on the surface of the carbon nanotubes hence the formation of heterostructures as shown in Fig. 6 (d-f).

Scanning Transmission Electron microscopy (STEM) is a technique used to determine the site-specific analysis of an image's resolution in the nanometer and sub-nanometer range. During this characterization, a dark field STEM image or bright field STEM picture can be formed basing on the transmitted electrons used during the formation of the image. Zhu et al. [64] used Titanium dioxide nanofibers-SnO_2 nanocubes as photoanode for dye-sensitized solar cells Fig. 7.

The scanning transmission electron microscopy shows an image and the corresponding EDS mapping for Sn, Ti, and O. It is observed that Sn and O have broader distributions compared to Ti and further gives information about the SnO_2 nanocubes which are connected to the TiO_2 nanofibers.

X-ray diffraction (XRD) is one of the most applied characterization techniques when it comes to structural determination of nanomaterials during DSSCs fabrication. Its working principle is based on Braggs law and X-rays from monochromatic light. Diffraction of the x-ray from the crystal structure of the material depends on the interplanar distance, scattering angle, and wavelength as shown in (Equation 6).

$$2d \sin \theta = n\lambda \tag{6}$$

Where d is the lattice spacing, θ represents the incident angle, λ is the wavelength, and n is the diffraction order. This technique gives information regarding the crystallinity of the material ie high peaks represent highly crystalline surfaces while broad peaks describe amorphous surfaces which are then compared with the International Centre for Diffraction Data (ICDD). Ahmad et al. [65] used XRD analysis (Fig. 8) to determine the crystalline structure of titanium dioxide nanoparticles.

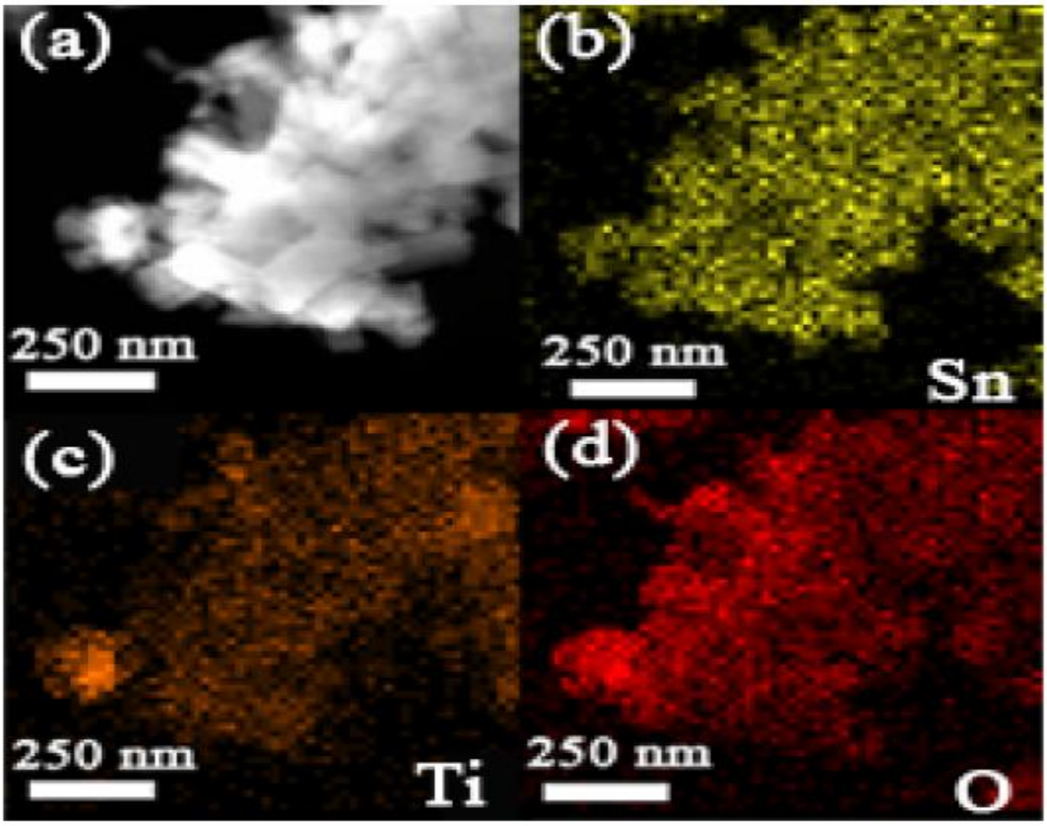

Fig. 7. STEM image of the nanofibers and the corresponding EDS mapping of Sn, Ti, and O [64]

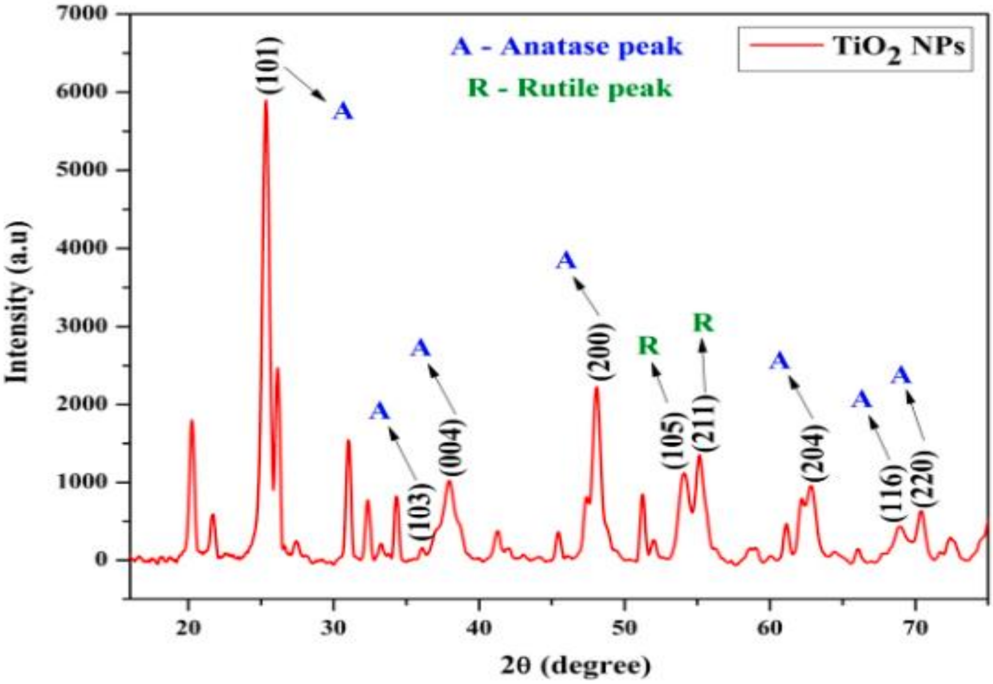

Fig. 8. XRD spectra of TiO_2 nanoparticles containing Anatase and Rutile phases [65]

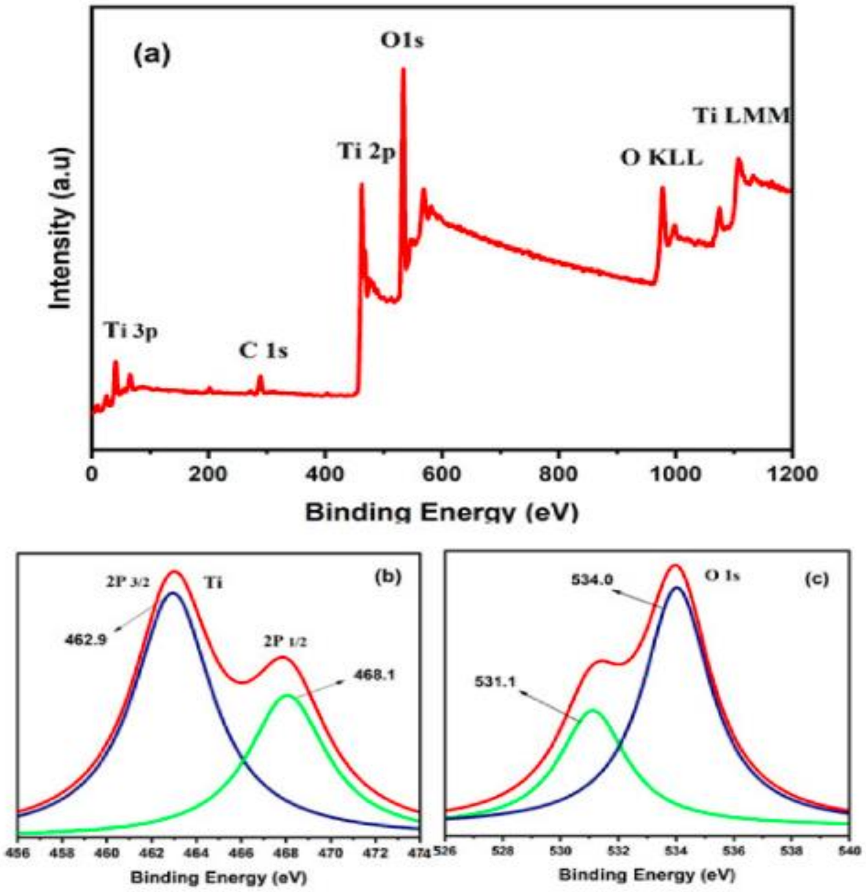

Fig. 9. XPS analysis of Titanium dioxide nanoparticles [66]

The 2θ were observed at 25.33, 36.01, 37.90, 48.06, 53.96, 55.06, 62.70, 69.01, and 70.41° which correspond to planes (101), (103), (004), (200), (105), (211), (204), (116) and (200) which mainly describe the anatase and rutile phase. From this analysis, the (101) plane had the strongest diffraction peak at 25.33° which is due to the Anatase form which is the most dominant in the titanium dioxide. The rutile form was also observed at 53.96 and 55.06°.

X-ray Photoelectron spectroscopy (XPS) uses x-rays to stimulate photoelectrons that determine surface depths up to about 10 nm. This technique has been observed to determine bigger particles within 100 nm. Khalid et al. [66] used XPS analysis (Fig. 9) to determine the electronic structure, valence states, and bonding properties of titanium dioxide nanoparticles.

The Ti 2p and O 1s are observed with no contamination but the C 1s are also observed at 285 eV [67]. The binding energy of the elements is determined and the spin states of Ti $2p_{3/2}$ and Ti $2p_{1/2}$ at binding energies of 463 eV and 468 eV for Ti^{4+} in TiO_2 are also determined which explains that Ti exists in the same oxidation state [68].

Fourier Transform Infrared Spectroscopy (FTIR) is another characterization technique that is used to determine the surface functional groups and optical properties of a variety of samples in the spectral region which ranges from 4000 – 400 cm^{-1}. Nanomaterials have atoms that vibrate at frequencies that are within the spectral range of FTIR. Guan et al. [69] analyzed pure TiO_2 and TiO_2-Ni nanocomposite using FTIR is used to determine the surface functional groups (Fig. 10). The bands at 662 and 704 cm^{-1} are characteristic of Ti-O vibrations in the lattice structure of TiO_2. A broad band in the region between 3000-3500 cm^{-1} is due to the surface hydroxyl groups and the stretching vibration on the TiO_2 surface but also a band around 1000-1700 cm^{-1} is due to the water molecule (H-O-H) with bending vibrations [70]. Ti-O-Ti vibrations are also observed with a broad band in the region of 1000-1200 cm^{-1}.

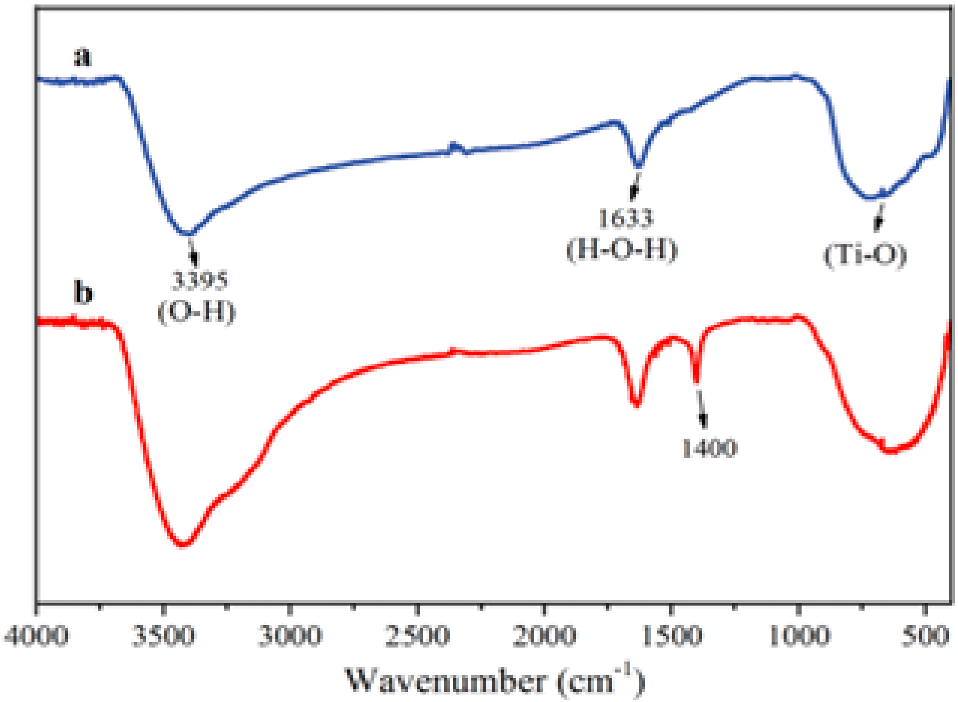

Fig. 10. FTIR spectrum of a) TiO_2 nanoparticles and b) TiO_2-Ni nanocomposite [69]

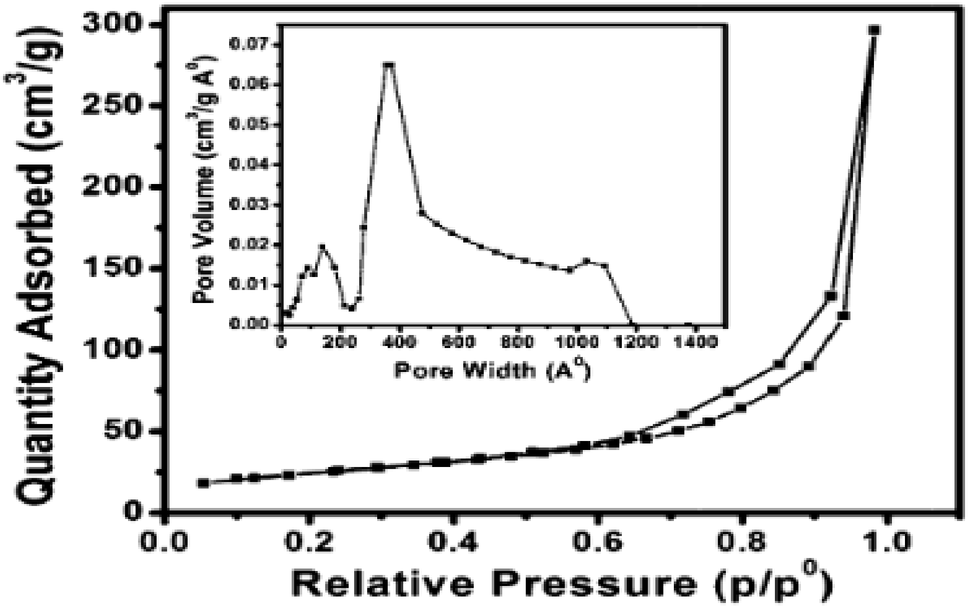

Fig. 11. Nitrogen desorption-adsorption isotherm of TiO_2 showing the pore volume insert [71]

Brunauer-Emmett-Teller (BET) analysis is used on the principle of physio-sorption of gas on a solid surface to determine the pore volume, surface area, and pore size of different materials. The gas that is normally used for the desorption and adsorption on solid surfaces is Nitrogen. This technique is considered a modification of the Langmuir adsorption as it considers multiple-layer adsorption. Pai et al [71] analyzed TiO_2 nanoparticles using BET as shown in Fig. 11. The surface area of the nanoparticles was estimated to be 86 m^2 g^{-1}, the pore volume was

0.46 $cm^3 g^{-1}$ and the pore size was about 212 Å which parameters aid in dye absorption onto the semiconductor.

TGA is a technique that is used to determine the composition, thermal stability, decomposition, kinetics of chemical reactions, and evaporation behavior of a material when a varying temperature is applied. Bekele et al. [72] analyzed TiO_2 nanoparticles for their stability and energy absorption using Thermal Gravimetric-Differential Thermal Analysis (TGA-DTA) Fig. 12. The TGA curve shows the weight loss of the TiO_2 nanoparticles while the DTA curve shows the energy gain or loss during the whole process. The weight loss at 150 °C is mainly due to the loss of water molecules, 350 °C is due to carbonization and pyrolysis of biomass. Further at 483 °C the weight loss corresponds to strong DTA peaks due to vaporization of residues and at 500 °C no weight loss was observed and this is taken as the carbonization temperature.

RAMAN is a technique that uses vibrational modes to determine the phase, polymorphy, crystallinity, chemical structure, and molecular interactions of a sample which occurs when light from the laser interacts with the material's chemical bonds. Khalid et al. [66] studied the spectrum of titanium dioxide nanoparticles using Raman spectroscopy as shown in Fig. 13.

It shows B_{1g}, (A_{1g} + B_{1g}), and E_g peaks at 399, 516, and 637 cm^{-1} [73,74]. The vibrational modes in TiO_2 are caused by bending, asymmetric, and symmetric vibrations of the Ti-O-TiO bond [75,76] The B_{1g} peak corresponds to Ti-O bending mode where the Ti-O-Ti (Ti is moving), A_{1g} + B_{1g} Ti-O stretching mode (O is moving) and E_g is the Ti-O stretching mode [77].

UV-VIS is used to measure the optical spectral properties of materials through light absorption of samples that are in solution. Using Beer Lambert's law this characterization technique gives information regarding the concentration and composition of a sample. It is also easy to operate, cheap, and does not destroy the sample after analysis. Camposeco et al. [78] used UV-Vis spectroscopy to study the optical properties of different Titanium dioxide nanostructures as shown in Fig. 14.

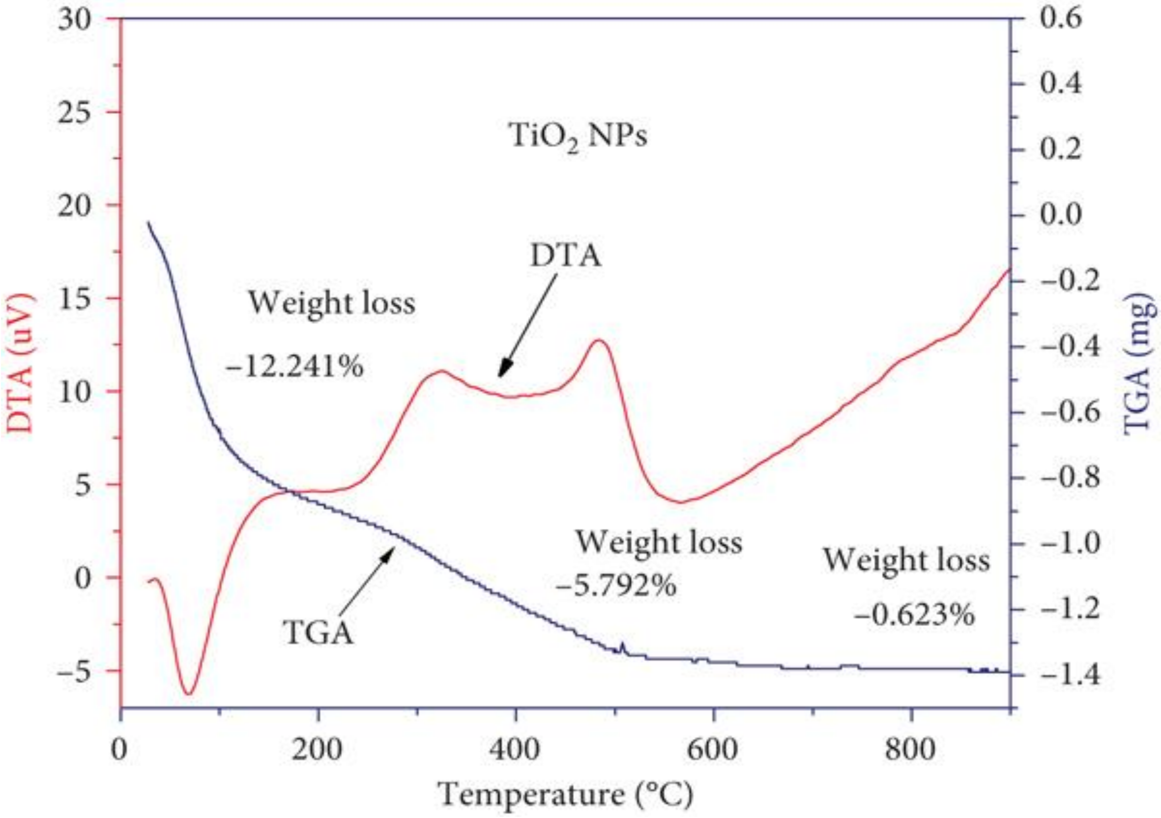

Fig. 12. TGA/DSC analysis of TiO_2 nanoparticles [72]

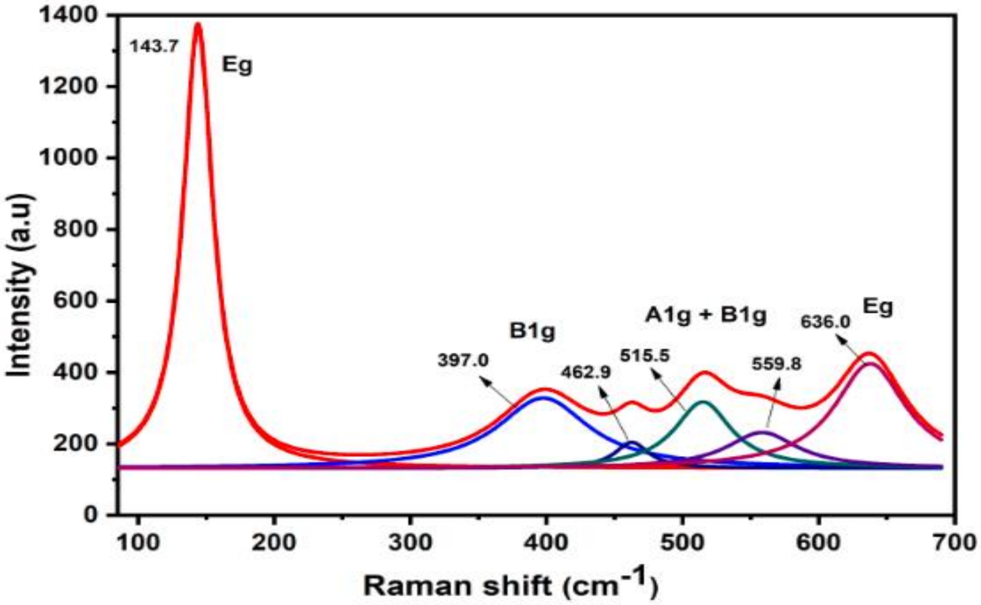

Fig. 13. Raman spectrum of Titanium dioxide nanoparticles [66]

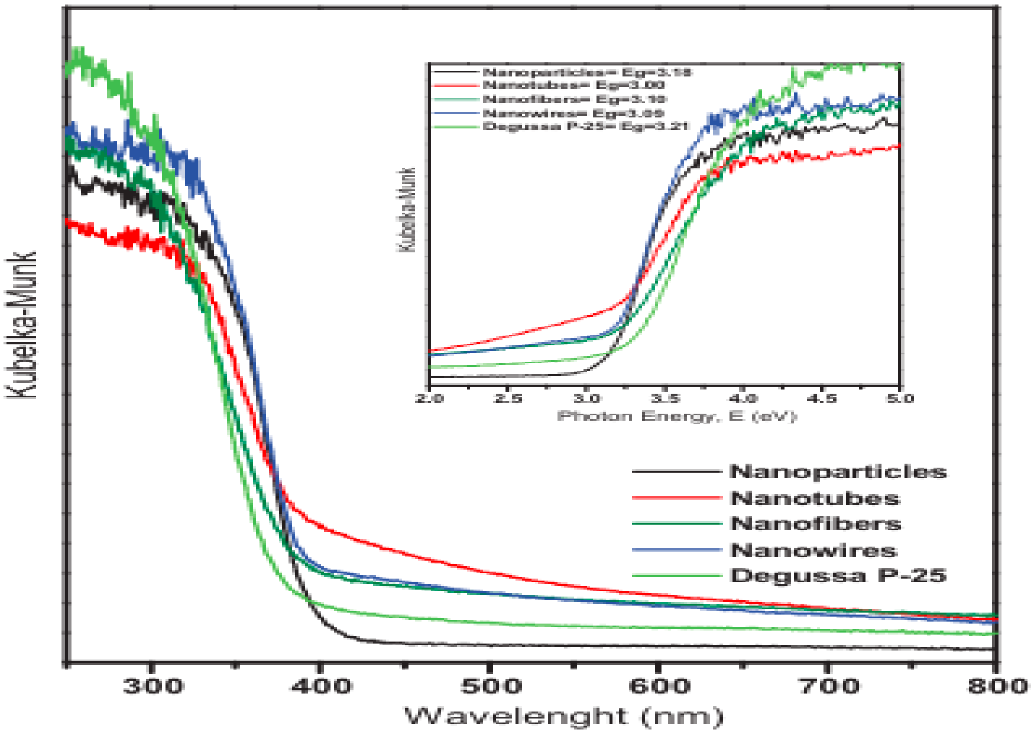

Fig. 14. UV-Vis spectrum of nanoparticles, nanotubes, nanofibers, nanowires, and P-25. Reprinted with permission ref [78]. Copyright 2016, Elsevier

It is observed that the anatase form of titanium dioxide has an absorption of 380-459 nm with an energy band gap (Eg) of 3.2 eV. The nanotubes have an observable red shift towards the visible light region of the spectrum which is mainly attributed to the synthesis method and temperature [79]. Insert Figure UV-Vis spectra showed the energy band gap (eV) of the nanoparticles (3.18), nanofibers (3.10), nanotubes (3.0), and nanowires (3.09).

4. TIO$_2$ NANOFIBERS, NANOWIRES, NANOTUBES, NANOPARTICLES, AND THEIR APPLICATION IN DSSCS

Titanium dioxide is known to exhibit four polymorphic forms which include anatase, rutile, brookite, and TiO$_2$ (B) [80]. It also has other polymorphs that are metastable such as perovskite, TiO$_2$ II, and TiO$_2$ (H) which are normally synthesized using synthetical pathways that require certain conditions. The most stable form is rutile while anatase and brookite are known to transform to rutile at high-temperature conditions which also affects titanium nanostructure formation [81,82]. Fig. 15 shows the crystal forms of the unit cells of the four most common titanium dioxide polymorphs [83].

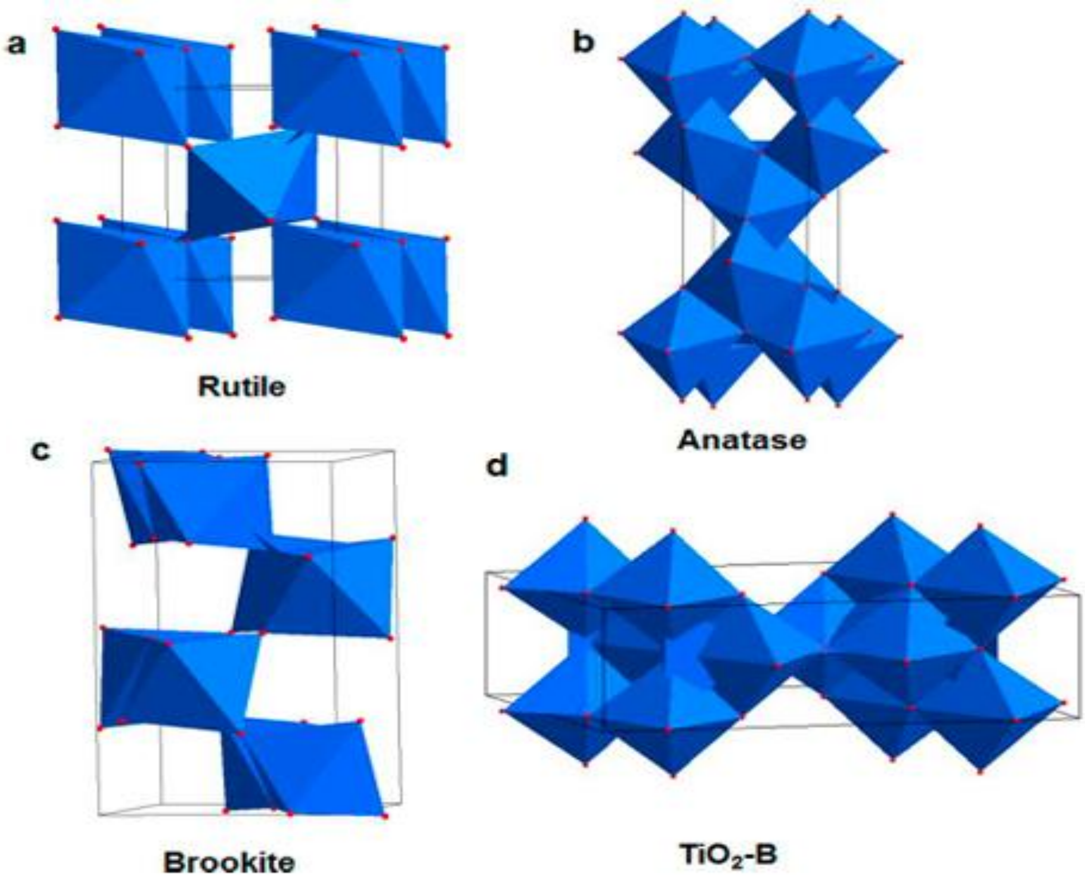

Fig. 15. A schematic unit cell of titanium dioxide crystal forms (a) Rutile, (b) Anatase, (c) Brookite, and (d) TiO$_2$ B) [83]

Table 1. Structural parameters of the crystal forms of titanium dioxide [85]

Parameter	Rutile	Brookite	Anatase
Unit cell	2	4	8
Atomic spacing (Å)	a = 4.596 c = 2.958	a = 9.184 b = 5.447 c = 5.145	a = 3.784 c = 9.515
Density (g/cm^3)	4.13	3.99	3.79
Bond Length Ti-O (Å)	1.949 (4) 1.980 (2)	1.87-2.04	1.937 (4) 1.965 (2)
Bond Angle O-Ti-O (Å)	81.2° 90.0°	77.0-105°	77.7° 92.6°

The Ti-O octahedron is known to be the fundamental building block of all the four crystal forms of TiO_2 which influences its symmetry. The nanostructures of these polymorphs tend to exhibit different morphologies and growth behaviors. Rutile has a tetragonal structure with a-axis (0.459 nm) and c-axis (0.296 nm), anatase also has a tetragonal structure with a-axis (0.379 nm) and c-axis (0.951 nm). Brookite has 8 TiO_2 groups containing large cell units which results in an orthorhombic structure. TiO_2 B has a monoclinic structure which is more open with large cell units and consists of long a-axis (1.216 nm) [84]. Table 1 shows the detailed structural parameters of Rutile, Brookite, and Anatase [85].

Titanium dioxide nanostructures are synthesized using a number of techniques such as hydrothermal treatment, chemical and physical vapor deposition, sputtering, sonochemical, template method, pulse laser ablation, electrodeposition, sol-gel, micro-emulsion, etc [86–89]. Synthesis of the nanostructures is based on a number of precursors such as titanium tetrachloride ($TiCl_4$), titanium isopropoxide (TTIP), titanium trichloride ($TiCl_3$) and titanium tetrabutoxide (TBT) [90–92].

A number of Titanium dioxide nanostructures such as 0D, 1D, 2D, and 3D architectures have been applied to determine their influence on the conversion efficiency of the dye-sensitized solar cells as shown in Fig. 16 [93].

The 0D nanostructures have a sphere or quasi-sphere shape and have diameters less than 100 nm. They have a high surface-to-volume ratio, less toxic, high quantum yield, and a number of active sites per unit mass [94]. The common members are the noble metal nanoparticles [95], carbon quantum dots [96], polymer dots [97], graphene quantum dots [98] and the fullerenes [99].

In addition, the 1D nanostructures have a high length-to-diameter ratio which improves the chemical, magnetic, and mechanical properties of the materials. They also have a large surface area, highly uniform, crystalline, and hollow which all enable their application in energy devices [100,101]. They include nanowires, nanotubes, nanorods, and nanofibers.

Furthermore, the 2D nanostructures whose atom layer thick planar structures are each bonded using weak van der waal forces [102]. The in plane covalent nature of the 2D structures leads to its robust nature and good mechanical stability [103]. The nanosheets [104] and nanoflakes [105] belong to this group of nanostructures.

Lastly the the 3D nanostructures whose organization, arrangement, and formation are developed using the 0D, 1D, and 2D materials. The morphologies are achieved based on the growth conditions. Among the 3D nanostructures, popular examples include nanoflowers [106], nanospheres [107], nanocubes [108], nanocages [109], dendrimers [110] and fullerenes [111].

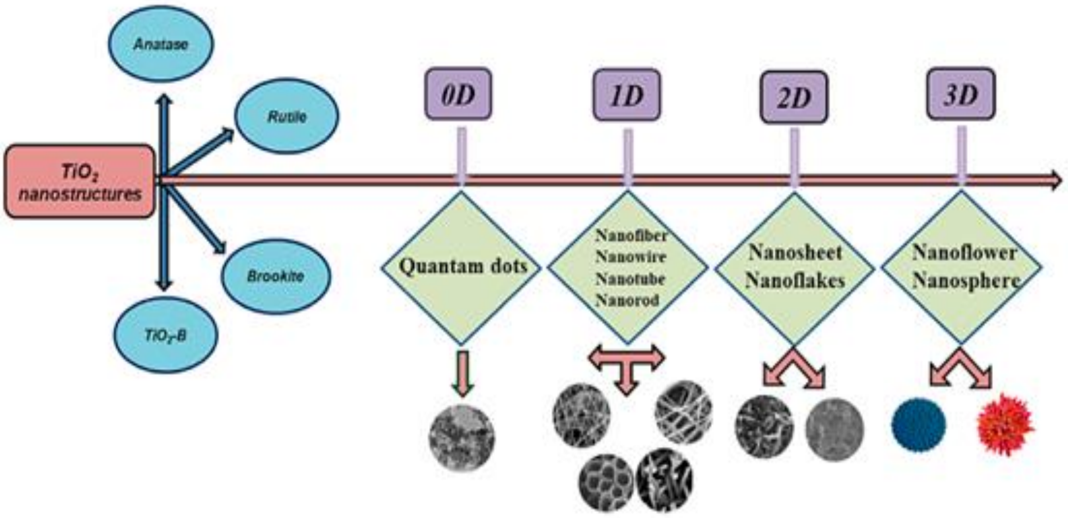

Fig. 16. Titanium dioxide nanostructures and the different dimensions [93]

Table 2. One-dimensional structures and the commonly used synthesis techniques

1D TiO_2 Nanostructures	Synthesis Technique
Nanotubes (NTs)	Electrochemical deposition, sol-gel, hydrothermal
Nanowires (NWs)	Solvothermal, microwave-assisted, sol-gel, hydrothermal
Nanorods (NRs)	Sol-gel template, hydrothermal, chemical vapor deposition
Nanofibers (NFs)	Hydrolysis, hydrothermal, electrospinning + sol-gel

Table 3. Performance of titanium dioxide nanowires and nanocomposite photoanodes

Electrode	J_{sc} (mA/cm^2)	V_{oc} (V)	η (%)	FF	Reference
TiO_2 NWs	17.38	0.687	8.90	0.75	[113]
Sn-TiO_2	15.84	0.755	8.75	0.73	[114]
TiO_2 NWs-TiO_2 NPs	14.02	0.762	7.92	0.74	[115]
TiO_2 NWs-RGO	10.41	0.714	4.95	0.67	[116]

Table 4. Performance of titanium dioxide nanoparticle and nanocomposite photoanodes

Electrode	J_{sc} (mA/cm^2)	V_{oc} (V)	η (%)	FF	Reference
TiO_2	9.68	0.732	9.34	0.70	[118]
TiO_2-rGO	12.57	0.761	6.64	0.54	[119]
TiO_2 (NRs-NP)	17.22	0.690	8.61	0.72	[120]
Cu-TiO_2NP-Graphene	19.93	0.745	9.81	0.66	[121]
TiO_2 NP-ZnO Nanorod	14.20	0.704	6.50	0.65	[122]

Table 5. Performance of titanium dioxide nanotubes and nanocomposite photoanodes

Electrode	J_{sc} (mA/cm^2)	V_{oc} (V)	η (%)	FF	Reference
TiO_2 TNTs	18.41	0.69	8.19	0.64	[127]
N-TiO_2 NTs	19.29	0.70	7.36	0.55	[128]
TNT-rGO	10.70	0.78	5.33	0.64	[129]
Ag-TNTs	17.26	0.78	7.20	0.54	[130]
Cr-TNTs	26.29	0.69	11.05	0.61	[127]

Table 6. Performance of titanium dioxide nanofibers and nanocomposite photoanodes

Electrode	J_{sc} (mA/cm^2)	V_{oc} (V)	η (%)	FF	Reference
TiO_2 NFs	9.70	0.812	5.1	0.65	[134]
Ag NPs-TiO_2 NFs	11.24	0.789	6.19	0.69	[135]
GO-TiO_2 NFs	9.41	0.784	4.52	0.61	[136]
SnO_2-TiO_2	17.00	0.732	8.0	0.64	[134]
TiO_2 NFs-TiO_2 NPs	14.46	0.750	7.13	0.65	[137]

The 1D nanostructures have found wide application in dye-sensitized solar due to their large surface area, good electronic properties, ease of fabrication, good chemical stability, and high aspect ratio as shown in Table 2 [93,112].

Titanium dioxide nanowires are the most applied 1D nanostructures in dye sensitized solar cells due to their large surface area which favors dye loading and anchorage. Table 3 shows Titanium dioxide nanowires, their composites, and how they influence DSSCs performance.

H. Li et al [113] synthesized pure Titanium dioxide nanowires as photoanodes for DSSCs and obtained an efficiency of 8.90 %. This is attributed to the high Jsc (17.38 mA/cm^2) which enables high light scattering and harvesting but also improves dye loading. Makal & Das [116] synthesized Reduced graphene oxide-titanium dioxide nanowires as photoanodes and obtained an efficiency of 4.95 % which is lower than pure TiO_2 (8.90 %) due to a lower Jsc 10.41 mA/cm^2. Reduced graphene oxide increases the rate of electron transfer but also inhibits the electron-hole charge carrier recombination. Another group of Ni et al [114] synthesized Titanium dioxide-doped Sn nanowires as photoanodes for DSSCs and the conversion efficiency was 8.75 %. The high J_{sc} increases the light-harvesting ability of the photoanode [117]. Wu et al [115] synthesized Titanium dioxide nanowires-Titanium dioxide nanoparticles as photoanodes for DSSCs and the efficiency obtained was 7.92 %. This is attributed to the high J_{sc} 14.02 mA/cm^2 which improves the light scattering ability but also on the dye loading onto the photoanode.

Titanium dioxide nanoparticles were studied to understand their effect on the overall performance of the DSSCs. Table 4 shows the photochemical parameters of TiO_2, TiO_2-rGO, TiO_2 (NRs-NP), Cu-TiO_2NP-Graphene and TiO_2 NP-ZnO Nanorod.

Dhonde et al [121] demonstrated the use of Cu-TiO_2NP-Graphene as photoanodes and they showed a conversion efficiency of 9.81 % comparable to that of TiO_2 (9.34 %). This is because Cu doping improves on V_{oc} (0.745 V) but also reduces the energy band gap of TiO_2 [123,124]. In addition, graphene improves the J_{sc} (19.93 mA/cm^2) as it improves dye loading, charge separation, and electron mobility and reduces the electron-hole charge carrier recombination [125]. Furthermore, Chatterjee et al [120] used TiO_2 (NR-NP) as photoanodes for DSSCs and the conversion efficiency was 8.61 % which is also comparable to that of TiO_2 (9.68 %). This is because the nanorod-nanoparticle composite increases the J_{sc} (17.22 mA/cm^2) of the DSSCs through improvement in the dye loading and light scattering which increases the efficiency [126]. Further studies by Zatirostami [122] demonstrated the use of TiO_2 NPs-ZnO nanorods and the conversion efficiency was 6.50 % which is comparable to TiO_2 (9.34 %). This was due to the hierarchical structure of the ZnO nanorods but also the high porosity of TiO_2 nanoparticles which improved dye loading, light scattering, and diffusion of the electrolyte into the semiconductor.

Nanotubes have also been studied in the determination of the conversion efficiency and performance of dye-sensitized solar cells. The Titanium dioxide nanotubes and their composites have shown great application as photoanodes in DSSCs application with relatively high efficiencies as shown in Table 5.

Nguyen et al [127] used Cr-TNTs as photoanodes and the conversion efficiency was 11.05 % which is higher than that of the undoped TiO_2 nanotubes. This is because of the high J_{sc} (26.29 mA/cm^2) which is due to the heterostructure of the TiO_2 nanotubes that causes a high dye-loading ability [131,132]. The oxygen vacancy sites due to doping cause the creation of holes which reduce the charge recombination. The Cr^{3+} and Ti^{3+} can also become defect centers in which they end up holding dye molecules on the composite which further influences the efficiency. In addition, Tran et al [128] used N-TiO_2 NTs as photoanodes and the conversion efficiency was 7.36 % which is comparable to that of undoped TiO_2 (8.19 %). This is also due to the increase in J_{sc} (19.29 mA/cm^2) which is a result of high electron injection into the reduced conduction band of the semiconductor but also the reduction in the electrolyte charge recombination [133].

Lastly, the Nanofibers have been applied as photoanodes in dye-sensitized solar cells. Table 6 shows some of the Titanium dioxide nanofibers that have shown good conversion efficiencies when used as photoanodes.

Bakr et al [134] used SnO_2-TiO_2 as photoanodes and the conversion efficiency was 8.0 % which is slightly higher than that of bare TiO_2 nanofibers (5.1 %). This is because of the high J_{sc} (17.00 mA/cm^2) which is due to the SnO_2 network which improved the surface area, electron transport, and dye loading onto the nanofibers. In addition, Vu et al [137] used TiO_2 NFs-TiO_2 NPs as photo anodes during DSSCs study and the efficiency was 7.13 % which is higher than that of TiO_2 (5.1 %). This is because of the increased J_{sc} (14.46 mA/cm^2) which is due to the improved light harvesting and scatting ability of the Titanium dioxide nanofibers [138].

5. CONCLUSION

Dye-sensitized solar cells convert solar to electric energy through the use of different components including the photoanode. It functions as an anchorage onto which the dye sensitizer is attached but also transfers electrons to the external circuit. The efficiency of the photoanode as observed is greatly affected by the short circuit current (J_{sc}) that is an increase in J_{sc} leads to a high efficiency. Titanium dioxide nanostructures are commonly used photoanode in dye-sensitized solar cells due to their large surface area which improves dye loading and the overall efficiency (12%). Titanium dioxide nanowires, nanotubes, nanoflowers, nanoribbons, nano-onions, nanoflakes, and nanofibers are used as photoanodes achieving efficiencies that are comparable to nanoparticles (12 %). The titanium nanotubes are observed to have high efficiencies of 11.05 % which are mainly due to their heterostructure and large surface area which allows dye loading and electron transfer. The nanowires also offer high efficiencies of 8.90 % which is also due to the large surface area for dye loading and photon absorption and scattering. Furthermore, the nanofibers with efficiencies of 8.0 % which are accounted for by the high J_{sc} values, and dye loading have seen rapid growth. Lastly, the characterization of these nanostructures has been reviewed using a number of techniques to understand the crystal orientation, morphology, surface functional groups, surface area, elemental composition, and other physical and chemical properties. In brief, this review confirms that the nanotubes, nanofibers, and nanowires are ideal candidates to be applied as photoanodes in DSSCs devices.

DISCLAIMER (ARTIFICIAL INTELLIGENCE)

Author (s) hereby declare that NO generative AI technologies such as Large Language Models (ChatGPT, COPILOT, etc) and text-to-image generators have been used during writing or editing of the manuscript.

ACKNOWLEDGEMENT

The authors acknowledge facilitation from Makerere University to access literature used in writing this review.

COMPETING INTERESTS

Authors have declared that no competing interests exist.

REFERENCES

1. Bbumba S, Karume I, Kigozi M, Oyege I, Ntale M. How Components of Dye-sensitized Solar Cells Contribute to Efficient Solar Energy Capture. Asian Journal of Applied Chemistry Research. 2024;15(2):24–40.
2. Shen S, Chen J, Wang M, Sheng X, Chen X, Feng X, et al. Titanium dioxide nanostructures for photoelectrochemical applications. Prog Mater Sci. 2018 Oct 1;98:299–385.
3. Aleklett K, Campbell CJ. The Peak and Decline of World Oil and Gas Production. Minerals & Energy - Raw Materials Report. 2003 Jan;18(1):5–20.
4. Nazeeruddin MK, Baranoff E, Grätzel M. Dye-sensitized solar cells: A brief overview. Solar Energy. 2011 Jun 1;85(6):1172–8.
5. Hagfeldt A, Boschloo G, Sun L, Kloo L, Pettersson H. Dye-Sensitized Solar Cells. Chem Rev. 2010 Sep 10;110(11):6595–663.

5a. Shen S, Chen J, Wang M, Sheng X, Chen X, Feng X, Mao SS. Titanium dioxide nanostructures for photoelectrochemical applications. Progress in Materials Science. 2018 Oct 1;98:299-385.

6. Fujishima A, Honda K. Electrochemical photolysis of water at a semiconductor electrode. Nature. 1972;238(5358): 37–8.
7. Umale S V., Tambat SN, Sudhakar V, Sontakke SM, Krishnamoorthy K. Fabrication, characterization and comparison of DSSC using anatase TiO2 synthesized by various methods. Advanced Powder Technology. 2017 Nov 1;28(11):2859–64.
8. Yeoh ME, Chan KY. Recent advances in photo-anode for dye-sensitized solar cells: a review. Int J Energy Res. 2017 Dec 1;41(15):2446–67.
9. O'Regan B, Grätzel M. A low-cost, high-efficiency solar cell based on dye-sensitized colloidal TiO2 films. Nature 1991 353:6346 [Internet]. 1991 Oct 24 [cited 2024 May 8];353(6346):737–40. Available from: https://www.nature.com/articles/353737a0
10. Roy P, Kim D, Lee K, Spiecker E, Schmuki P. TiO2 nanotubes and their application in dye-sensitized solar cells. Nanoscale. 2010;2(1):45–59.
11. Qin Y, Peng Q. Ruthenium Sensitizers and Their Applications in Dye-Sensitized Solar Cells. International Journal of Photoenergy; 2012.
12. Thomas S, Deepak TG, Anjusree GS, Arun TA, Nair S V, Nair AS. A review on counter electrode materials in dye-sensitized solar cells. J Mater Chem A Mater. 2014; 2(13):4474–90.
13. Kawashima T, Ezure T, Okada K, Matsui H, Goto K, Tanabe N. FTO/ITO double-layered transparent conductive oxide for dye-sensitized solar cells. J Photochem

Photobiol A Chem. 2004;164(1–3):199–202.

14. Bella F, Bongiovanni R. Photoinduced polymerization: an innovative, powerful and environmentally friendly technique for the preparation of polymer electrolytes for dye-sensitized solar cells. Journal of photochemistry and photobiology C: photochemistry reviews. 2013;16:1–21.
15. Tanaka K, Capule MFV, Hisanaga T. Effect of crystallinity of TiO2 on its photocatalytic action. Chem Phys Lett. 1991 Nov 29;187(1–2):73–6.
16. O'regan B, Grätzel M. A low-cost, high-efficiency solar cell based on dye-sensitized colloidal TiO2 films. Nature. 1991;353(6346):737–40.
17. Fessenden RW, Kamat P V. Rate constants for charge injection from excited sensitizer into SnO2, ZnO, and TiO2 semiconductor nanocrystallites. J Phys Chem. 1995;99(34):12902–6.
18. Bjoerksten U, Moser J, Graetzel M. Photoelectrochemical studies on nanocrystalline hematite films. Chemistry of materials. 1994;6(6):858–63.
19. Rensmo H, Keis K, Lindström H, Södergren S, Solbrand A, Hagfeldt A, et al. High light-to-energy conversion efficiencies for solar cells based on nanostructured ZnO electrodes. J Phys Chem B. 1997; 101(14):2598–601.
20. Hotchandani S, Kamat P V. Photoelectrochemistry of semiconductor ZnO particulate films. J Electrochem Soc. 1992;139(6):1630.
21. Kakiage K, Aoyama Y, Yano T, Otsuka T, Kyomen T, Unno M, et al. An achievement of over 12 percent efficiency in an organic dye-sensitized solar cell. Chemical Communications. 2014;50(48):6379–81.
22. Graetzel M, Janssen RAJ, Mitzi DB, Sargent EH. Materials interface engineering for solution-processed photovoltaics. Nature. 2012;488(7411): 304–12.
23. Zhang X, Liu F, Huang QL, Zhou G, Wang ZS. Dye-sensitized W-doped TiO2 solar cells with a tunable conduction band and suppressed charge recombination. The journal of physical chemistry C. 2011; 115(25):12665–71.
24. Wang Y, Hao Y, Cheng H, Ma J, Xu B, Li W, et al. The photoelectrochemistry of transition metal-ion-doped TiO2 nanocrystalline electrodes and higher solar cell conversion efficiency based on Zn2+-doped TiO2 electrode. J Mater Sci. 1999;34:2773–9.
25. Lü X, Mou X, Wu J, Zhang D, Zhang L, Huang F, et al. Improved-performance dye-sensitized solar cells using Nb-doped TiO2 electrodes: efficient electron injection and transfer. Adv Funct Mater. 2010; 20(3):509–15.
26. Zhang J, Zhao Z, Wang X, Yu T, Guan J, Yu Z, et al. Increasing the oxygen vacancy density on the TiO2 surface by La-doping for dye-sensitized solar cells. The Journal of Physical Chemistry C. 2010;114(43): 18396–400.
27. Song J, Yang H Bin, Wang X, Khoo SY, Wong CC, Liu XW, et al. Improved utilization of photogenerated charge using fluorine-doped TiO2 hollow spheres scattering layer in dye-sensitized solar cells. ACS Appl Mater Interfaces. 2012; 4(7):3712–7.
28. Chu D, Yuan X, Qin G, Xu M, Zheng P, Lu J, et al. Efficient carbon-doped nanostructured TiO 2 (anatase) film for photoelectrochemical solar cells. Journal of Nanoparticle Research. 2008;10:357–63.
29. Kang SH, Kim HS, Kim JY, Sung YE. Enhanced photocurrent of nitrogen-doped TiO2 film for dye-sensitized solar cells. Mater Chem Phys. 2010;124(1):422–6.
30. Ma T, Akiyama M, Abe E, Imai I. High-efficiency dye-sensitized solar cell based on a nitrogen-doped nanostructured titania electrode. Nano Lett. 2005;5(12):2543–7.

30a. Órdenes-Aenishanslins NA, Saona LA, Durán-Toro VM, Monrás JP, Bravo DM, Pérez-Donoso JM. Use of titanium dioxide nanoparticles biosynthesized by Bacillus mycoides in quantum dot sensitized solar cells. Microbial cell factories. 2014 Dec;13:1-0.

31. Sun Q, Zhang J, Wang P, Zheng J, Zhang X, Cui Y, et al. Sulfur-doped TiO2 nanocrystalline photoanodes for dye-sensitized solar cells. Journal of Renewable and Sustainable Energy. 2012;4(2).
32. Jose R, Thavasi V, Ramakrishna S. Metal oxides for dye-sensitized solar cells. Journal of the American Ceramic Society. 2009;92(2):289–301.
33. Hamann TW, Ondersma JW. Dye-sensitized solar cell redox shuttles. Energy

Environ Sci [Internet]. 2011;4(2):370–81. Available:http://dx.doi.org/10.1039/C0EE00251H

34. Al-Alwani MAM, Mohamad AB, Ludin NA, Kadhum AAH, Sopian K. Dye-sensitised solar cells: Development, structure, operation principles, electron kinetics, characterisation, synthesis materials and natural photosensitisers. Renewable and Sustainable Energy Reviews. 2016;65: 183–213.
35. Jose R, Kumar A, Thavasi V, Fujihara K, Uchida S, Ramakrishna S. Relationship between the molecular orbital structure of the dyes and photocurrent density in the dye-sensitized solar cells. Appl Phys Lett. 2008;93(2).
36. Bisquert J. Theory of the impedance of electron diffusion and recombination in a thin layer. J Phys Chem B. 2002;106(2):325–33.
37. Fabregat-Santiago F, Garcia-Belmonte G, Bisquert J, Zaban A, Salvador P. Decoupling of transport, charge storage, and interfacial charge transfer in the nanocrystalline TiO2/electrolyte system by impedance methods. J Phys Chem B. 2002;106(2):334–9.
38. Hagfeldt A, Boschloo G, Sun L, Kloo L, Pettersson H. Dye-sensitized solar cells. Chem Rev. 2010;110(11):6595–663.
39. Lasia A. Electrochemical impedance spectroscopy and its applications. In: Modern aspects of electrochemistry. Springer; 2002. p. 143–248.
40. Sacco A. Electrochemical impedance spectroscopy: Fundamentals and application in dye-sensitized solar cells. Renewable and Sustainable Energy Reviews. 2017 Nov 1;79:814–29.
41. Huang Z, Natu G, Ji Z, Hasin P, Wu Y. p-type dye-sensitized NiO solar cells: a study by electrochemical impedance spectroscopy. The Journal of Physical Chemistry C. 2011;115(50):25109–14.
42. Saranya K, Rameez M, Subramania A. Developments in conducting polymer based counter electrodes for dye-sensitized solar cells–An overview. Eur Polym J. 2015;66:207–27.
43. Pitarch Á, Garcia-Belmonte G, Mora-Seró I, Bisquert J. Electrochemical impedance spectra for the complete equivalent circuit of diffusion and reaction under steady-state recombination current. Physical Chemistry Chemical Physics. 2004;6(11): 2983–8.
44. Bisquert J, Garcia-Belmonte G, Fabregat-Santiago F, Ferriols NS, Bogdanoff P, Pereira EC. Doubling exponent models for the analysis of porous film electrodes by impedance. Relaxation of TiO2 nanoporous in aqueous solution. J Phys Chem B. 2000;104(10):2287–98.
45. Adachi M, Sakamoto M, Jiu J, Ogata Y, Isoda S. Determination of parameters of electron transport in dye-sensitized solar cells using electrochemical impedance spectroscopy. J Phys Chem B. 2006; 110(28):13872–80.
46. Kern R, Sastrawan R, Ferber J, Stangl R, Luther J. Modeling and interpretation of electrical impedance spectra of dye solar cells operated under open-circuit conditions. Electrochim Acta. 2002;47(26): 4213–25.
47. Nazeeruddin MK, Baranoff E, Grätzel M. Dye-sensitized solar cells: A brief overview. Solar energy. 2011;85(6):1172–8.
48. Hagfeldt A, Boschloo G, Sun L, Kloo L, Pettersson H. Dye-sensitized solar cells. Chem Rev. 2010;110(11):6595–663.
49. Grätzel M. Solar energy conversion by dye-sensitized photovoltaic cells. Inorg Chem. 2005;44(20):6841–51.
50. Mourdikoudis S, Pallares RM, Thanh NTK. Characterization techniques for nanoparticles: comparison and complementarity upon studying nanoparticle properties. Nanoscale. 2018;10(27):12871–934.
51. Birkholz M. Thin film analysis by X-ray scattering. John Wiley & Sons; 2006.
52. Engelhard MH, Droubay TC, Du Y. X-ray photoelectron spectroscopy applications. Pacific Northwest National Lab.(PNNL), Richland, WA (United States …; 2017.
53. Tahir MY, Ali S. Analytical techniques for nanomaterials. Nanomaterials-Based Electrochemical Sensors: Properties, Applications, and Recent Advances. 2024 Jan 1;37–51.
54. Mehrpouya M, Lavvafi H, Darafsheh A. Microstructural characterization and mechanical reliability of laser-machined structures. Advances in laser materials processing. 2018;731–61.
55. Darienzo RE, Wang J, Chen O, Sullivan M, Mironava T, Kim H, et al. Surface-Enhanced Raman Spectroscopy

Characterization of Breast Cell Phenotypes: Effect of Nanoparticle Geometry. ACS Appl Nano Mater. 2019;2(11):6960–70.

56. Bottom R. Thermogravimetric analysis. Principles and applications of thermal analysis. 2008;87–118.
57. Venkatachalam S. Ultraviolet and visible spectroscopy studies of nanofillers and their polymer nanocomposites. Spectroscopy of polymer nanocomposites. 2016;130–57.
58. Nasrollahzadeh M, Atarod M, Sajjadi M, Sajadi SM, Issaabadi Z. Plant-mediated green synthesis of nanostructures: mechanisms, characterization, and applications. In: Interface science and technology. Elsevier. 2019;199–322.
59. Janssens ML. Fundamental measurement techniques. In: Flammability Testing of Materials Used in Construction, Transport and Mining. Elsevier. 2022;23–61.
60. Lapresta-Fernández A, Salinas-Castillo A, Anderson De La Llana S, Costa-Fernández JM, Domínguez-Meister S, Cecchini R, et al. A general perspective of the characterization and quantification of nanoparticles: imaging, spectroscopic, and separation techniques. Critical Reviews in Solid State and Materials Sciences. 2014;39(6):423–58.
61. García-Negrete CA, de Haro MCJ, Blasco J, Soto M, Fernández A. STEM-in-SEM high resolution imaging of gold nanoparticles and bivalve tissues in bioaccumulation experiments. Analyst. 2015;140(9):3082–9.
62. Yao S, Tang H, Liu M, Chen L, Jing M, Shen X, et al. TiO2 nanoparticles incorporation in carbon nanofiber as a multi-functional interlayer toward ultralong cycle-life lithium-sulfur batteries. J Alloys Compd. 2019 Jun 5;788:639–48.
63. Li Y, Wang Z, Zhao H, Yang M. Composite of TiO2 nanoparticles and carbon nanotubes loaded on poly(methyl methacrylate) nanofibers: Preparation and photocatalytic performance. Synth Met. 2020 Nov 1;269:116529.
64. Zhu X, Jan SS, Zan F, Wang Y, Xia H. Hierarchically branched TiO2@ SnO2 nanofibers as high performance anodes for lithium-ion batteries. Mater Res Bull. 2017;96:405–12.
65. Ahmad MM, Mushtaq S, Al Qahtani HS, Sedky A, Alam MW. Investigation of TiO2 nanoparticles synthesized by sol-gel method for effectual photodegradation, oxidation and reduction reaction. Crystals (Basel). 2021;11(12):1456.
66. Khalid A, Ahmad P, Alharthi AI, Muhammad S, Khandaker MU, Iqbal Faruque MR, et al. Unmodified titanium dioxide nanoparticles as a potential contrast agent in photon emission computed tomography. Crystals (Basel). 2021;11(2):171.
67. Goktas A. High-quality solution-based Co and Cu co-doped ZnO nanocrystalline thin films: Comparison of the effects of air and argon annealing environments. J Alloys Compd. 2018;735:2038–45.
68. Muilenberg GE. Handbook of X-ray photoelectron spectroscopy. Perkin-Elmer; 1979.
69. Guan B, Yu J, Guo S, Yu S, Han S. Porous nickel doped titanium dioxide nanoparticles with improved visible light photocatalytic activity. Nanoscale Adv. 2020;2(3):1352–7.
70. Sharma R, Kar KK. Effects of structural disorder and nitrogen content on the oxygen reduction activity of polyvinylpyrrolidone-derived multi-doped carbon. J Mater Chem A Mater. 2015;3(22):11948–59.
71. Pai KRN, Anjusree GS, Deepak TG, Subash D, Nair S V, Nair AS. High surface area TiO 2 nanoparticles by a freeze-drying approach for dye-sensitized solar cells. RSC Adv. 2014;4(69):36821–7.
72. Bekele ET, Gonfa BA, Zelekew OA, Belay HH, Sabir FK. Synthesis of titanium oxide nanoparticles using root extract of Kniphofia foliosa as a template, characterization, and its application on drug resistance bacteria. J Nanomater. 2020;2020:1–10.
73. Ohsaka T, Izumi F, Fujiki Y. Raman spectrum of anatase, TiO2. Journal of Raman Spectroscopy. 1978;7(6):321–4.
74. Xu CY, Zhang PX, Yan L. Blue shift of Raman peak from coated TiO2 nanoparticles. Journal of Raman Spectroscopy. 2001;32(10):862–5.
75. Frank O, Zukalova M, Laskova B, Kürti J, Koltai J, Kavan L. Raman spectra of titanium dioxide (anatase, rutile) with identified oxygen isotopes (16, 17, 18). Physical Chemistry Chemical Physics. 2012;14(42):14567–72.

76. Choudhury B, Choudhury A. Room temperature ferromagnetism in defective TiO2 nanoparticles: Role of surface and grain boundary oxygen vacancies. J Appl Phys. 2013;114(20).
77. Li F, Gu Y. Improvement of performance of dye-sensitized solar cells by doping Er2O3 into TiO2 electrodes. Mater Sci Semicond Process. 2012;15(1):11–4.
78. Camposeco R, Castillo S, Navarrete J, Gomez R. Synthesis, characterization and photocatalytic activity of TiO2 nanostructures: Nanotubes, nanofibers, nanowires and nanoparticles. Catal Today. 2016 May 15;266:90–101.
79. Asahi R, Morikawa T, Ohwaki T, Aoki K, Taga Y. Visible-light photocatalysis in nitrogen-doped titanium oxides. Science (1979). 2001;293(5528):269–71.
80. Banfield JF, Veblen DR. Conversion of perovskite to anatase and TiO2 (B): A TEM study and the use of fundamental building blocks for understanding relationships among the TiO2 minerals. American Mineralogist. 1992;77(5–6):545–57.
81. Lee K, Mazare A, Schmuki P. One-dimensional titanium dioxide nanomaterials: nanotubes. Chem Rev. 2014;114(19):9385–454.
82. Pawar M, Topcu Sendoğdular S, Gouma P. A brief overview of TiO2 Photocatalyst for organic dye remediation: case study of reaction mechanisms involved in Ce-TiO2 Photocatalysts system. J Nanomater. 2018;2018(1):5953609.
83. Wang X, Li Z, Shi J, Yu Y. One-dimensional titanium dioxide nanomaterials: nanowires, nanorods, and nanobelts. Chem Rev. 2014;114(19):9346–84.
84. Marchand R, Brohan L, Tournoux M. TiO2 (B) a new form of titanium dioxide and the potassium octatitanate K2Ti8O17. Mater Res Bull. 1980;15(8):1129–33.
85. Mo SD, Ching WY. Electronic and optical properties of three phases of titanium dioxide: Rutile, anatase, and brookite. Phys Rev B. 1995;51(19):13023.
86. Nyamukamba P, Okoh O, Mungondori H, Taziwa R, Zinya S. Synthetic methods for titanium dioxide nanoparticles: a review. Titanium dioxide-material for a sustainable environment. 2018;8:151–75.
87. Mironyuk IF, Soltys LM, Tatarchuk TR, Savka KO. Methods of titanium dioxide synthesis. Physics and Chemistry of Solid State. 2020;21(3):462–77.
88. Aravind M, Amalanathan M, Mary MSM. Synthesis of TiO 2 nanoparticles by chemical and green synthesis methods and their multifaceted properties. SN Appl Sci. 2021;3:1–10.
89. Kamaludin R, Othman MHD, Kadir SHSA, Ismail AF, Rahman MA, Jaafar J. Visible-light-driven photocatalytic N-doped TiO 2 for degradation of bisphenol A (BPA) and reactive Black 5 (RB5) dye. Water Air Soil Pollut. 2018;229:1–11.
90. Joni IM, Nulhakim L, Vanitha M, Panatarani C. Characteristics of crystalline silica (SiO2) particles prepared by simple solution method using sodium silicate (Na2SiO3) precursor. In: Journal of Physics: Conference Series. IOP Publishing; 2018. p. 012006.
91. Singh PK, Mukherjee S, Ghosh CK, Maitra S. Influence of precursor type on structural, morphological, dielectric and magnetic properties of TiO 2 nanoparticles. Cerâmica. 2017;63:549–56.
92. Karkare MM. Choice of precursor not affecting the size of anatase TiO2 nanoparticles but affecting morphology under broader view. Int Nano Lett. 2014;4(3):111.
93. Reghunath S, Pinheiro D, KR SD. A review of hierarchical nanostructures of TiO2: Advances and applications. Applied Surface Science Advances. 2021;3:100063.
94. Wang Z, Hu T, Liang R, Wei M. Application of zero-dimensional nanomaterials in biosensing. Front Chem. 2020;8:320.
95. Bagheri N, Khataee A, Habibi B, Hassanzadeh J. Mimetic Ag nanoparticle/Zn-based MOF nanocomposite (AgNPs@ ZnMOF) capped with molecularly imprinted polymer for the selective detection of patulin. Talanta. 2018;179:710–8.
96. Sher F, Ziani I, Smith M, Chugreeva G, Hashimzada SZ, Prola LDT, et al. Carbon quantum dots conjugated with metal hybrid nanoparticles as advanced electrocatalyst for energy applications – A review. Coord Chem Rev. 2024 Feb 1;500:215499.
97. Dong J, Zhao J, Yan X, Li L, Liu G, Ji M, et al. Construction of carbonized polymer dots/potassium doped carbon nitride nanosheets Van der Waals heterojunction by ball milling method for facilitating

photocatalytic CO2 reduction performance in pure water. Applied Catalysis B: Environment and Energy. 2024 Aug 15;351:123993.

98. Dananjaya V, Marimuthu S, Yang R (Chunhui), Grace AN, Abeykoon C. Synthesis, properties, applications, 3D printing and machine learning of graphene quantum dots in polymer nanocomposites. Prog Mater Sci. 2024 Aug 1;144:101282.
99. Pesado-Gómez C, Serrano-García JS, Amaya-Flórez A, Pesado-Gómez G, Soto-Contreras A, Morales-Morales D, et al. Fullerenes: Historical background, novel biological activities versus possible health risks. Coord Chem Rev. 2024 Feb 15;501:215550.
100. Su B, Wu Y, Jiang L. The art of aligning one-dimensional (1D) nanostructures. Chem Soc Rev. 2012;41(23):7832–56.
101. Gholami T, Pirsaheb M. Review on effective parameters in electrochemical hydrogen storage. Int J Hydrogen Energy. 2021;46(1):783–95.
102. Fatima J, Shah AN, Tahir MB, Mehmood T, Shah AA, Tanveer M, et al. Tunable 2D nanomaterials; their key roles and mechanisms in water purification and monitoring. Front Environ Sci. 2022;10:766743.
103. Chhowalla M, Jena D, Zhang H. Two-dimensional semiconductors for transistors. Nat Rev Mater. 2016;1(11):1–15.
104. Ghai V, Pashazadeh S, Ruan H, Kádár R. Orientation of graphene nanosheets in magnetic fields. Prog Mater Sci. 2024 Jun 1;143:101251.
105. Shinde SK, Karade SS, Truong NTN, Veer SS, Shaikh SF, Al-Enizi AM, et al. Highly stable and thin layer of conducting PANI decorative on porous 3D nanoflakes like-NiCo2O4/CF nanomaterials for efficient Hybrid Supercapacitors application. J Energy Storage. 2024 Feb 1;78:109960.
106. Dai B, Hu Y, Ding Y, Shen L, Li R, Zhao D, et al. Innovative construction of nano-wrinkled polyamide membranes using covalent organic framework nanoflowers for efficient desalination and antibiotic removal. Desalination. 2024 Jan 15;570:117083.
107. Shreya, Phogat P, Jha R, Singh S. Carbon nanospheres-induced enhanced capacitive dynamics in C/WS2/WO3 nanocomposites for high-performance electrochemical capacitors. Materials Science and Engineering: B. 2024 Jun 1;304:117390.
108. Wang R, Jing Q, Li X, Wang S, Zhao Y, Wang H. Ag nanocubes-decorated ammonium hydroxide-treated carbon nitride to improve photocatalytic H2O2 production and fuel cell performance. J Power Sources. 2024 Jul 15;608:234654.
109. Chen Y, Zhu K, Qin W, Jiang Z, Hu Z, Sillanpää M, et al. Enhanced electron transfer using NiCo2O4@C hollow nanocages with an electron-shuttle effect for efficient tetracycline degradation. Chemical Engineering Journal. 2024 May 15;488:150786.
110. Grodzicka M, Michlewska S, Blasiak J, Ortega P, de la Mata FJ, Bryszewska M, et al. Polyphenolic dendrimers as carriers of anticancer siRNA. Int J Pharm. 2024 Jun 10;658:124199.
111. Paramasivam G, Palem VV, Sundaram T, Sundaram V, Kishore SC, Bellucci S. Nanomaterials: Synthesis and applications in theranostics. Nanomaterials. 2021;11(12):3228.
112. Feng T, Feng GS, Yan L, Pan JH. One-dimensional nanostructured TiO2 for photocatalytic degradation of organic pollutants in wastewater. International Journal of Photoenergy. 2014;2014(1):563879.
113. Li H, Yu Q, Huang Y, Yu C, Li R, Wang J, et al. Ultralong rutile TiO2 nanowire arrays for highly efficient dye-sensitized solar cells. ACS Appl Mater Interfaces. 2016;8(21):13384–91.
114. Ni S, Guo F, Wang D, Jiao S, Wang J, Zhang Y, et al. Modification of TiO2 nanowire arrays with Sn doping as photoanode for highly efficient dye-sensitized solar cells. Crystals (Basel). 2019;9(2):113.
115. Wu WQ, Liao JY, Chen HY, Yu XY, Su CY, Kuang DB. Dye-sensitized solar cells based on a double layered TiO2 photoanode consisting of hierarchical nanowire arrays and nanoparticles with greatly improved photovoltaic performance. J Mater Chem [Internet]. 2012;22(34):18057–62. Available from: http://dx.doi.org/10.1039/C2JM33829G
116. Makal P, Das D. Reduced graphene oxide-laminated one-dimensional TiO2–bronze nanowire composite: an efficient

photoanode material for dye-sensitized solar cells. ACS Omega. 2021;6(6):4362–73.

117. Snaith HJ, Ducati C. SnO2-based dye-sensitized hybrid solar cells exhibiting near unity absorbed photon-to-electron conversion efficiency. Nano Lett. 2010; 10(4):1259–65.
118. Ramakrishnan VM, Pitchaiya S, Muthukumarasamy N, Kvamme K, Rajesh G, Agilan S, et al. Performance of TiO2 nanoparticles synthesized by microwave and solvothermal methods as photoanode in dye-sensitized solar cells (DSSC). Int J Hydrogen Energy. 2020;45(51): 27036–46.
119. Pervaiz H, Shahzad N, Jamil Q. The impact of a TiO 2/r-GO composite material on the performance of electron transport electrodes of dye sensitized solar cells. RSC Adv. 2024;14(23):15907–14.
120. Chatterjee S, Webre WA, Patra S, Rout B, Glass GA, D’Souza F, et al. Achievement of superior efficiency of TiO2 nanorod-nanoparticle composite photoanode in dye sensitized solar cell. J Alloys Compd. 2020 Jun 15;826:154188.
121. Dhonde M, Sahu K, Murty VVS. Cu-doped TiO2 nanoparticles/graphene composites for efficient dye-sensitized solar cells. Solar Energy. 2021 May 15;220:418–24.
122. Zatirostami A. Fabrication of dye-sensitized solar cells based on the composite TiO2 nanoparticles/ZnO nanorods: Investigating the role of photoanode porosity. Mater Today Commun. 2021 Mar 1;26: 102033.
123. Aneesiya KR, Louis C. Localized surface plasmon resonance of Cu-doped ZnO nanostructures and the material’s integration in dye sensitized solar cells (DSSCs) enabling high open-circuit potentials. J Alloys Compd. 2020;829: 154497.
124. Vajda M, Ursu D, Duteanu N, Miclau M. Low lying valence band edge materials based on copper oxide for tandem dye-sensitized solar cells. Mater Lett. 2020 Sep 15;275:128151.
125. Sun Y, Wu Q, Shi G. Graphene based new energy materials. Energy Environ Sci. 2011;4(4):1113–32.
126. Jalali M, Moakhar RS, Kushwaha A, Goh GKL, Riahi-Noori N, Sadrnezhaad SK. Enhanced dye loading-light harvesting TiO2 photoanode with screen printed nanorod-nanoparticles assembly for highly efficient solar cell. Electrochim Acta. 2015;169:395–401.
127. Nguyen HH, Gyawali G, Hoon JS, Sekino T, Lee SW. Cr-doped TiO2 nanotubes with a double-layer model: An effective way to improve the efficiency of dye-sensitized solar cells. Appl Surf Sci. 2018 Nov 15;458:523–8.
128. Tran VA, Truong TT, Phan TAP, Nguyen TN, Huynh T Van, Agresti A, et al. Application of nitrogen-doped TiO2 nano-tubes in dye-sensitized solar cells. Appl Surf Sci. 2017 Mar 31;399:515–22.
129. Cai H, Li J, Xu X, Tang H, Luo J, Binnemans K, et al. Nanostructured composites of one-dimensional TiO2 and reduced graphene oxide for efficient dye-sensitized solar cells. J Alloys Compd. 2017;697:132–7.
130. Liu C, Li T, Zhang Y, Kong T, Zhuang T, Cui Y, et al. Silver nanoparticle modified TiO2 nanotubes with enhanced the efficiency of dye-sensitized solar cells. Microporous and Mesoporous Materials. 2019 Oct 1;287:228–33.
131. Mercado CC, Knorr FJ, McHale JL, Usmani SM, Ichimura AS, Saraf L V. Location of hole and electron traps on nanocrystalline anatase TiO2. The Journal of Physical Chemistry C. 2012;116(19) :10796–804.
132. Hao NH, Gyawali G, Sekino T, Lee SW. Fabrication of a TiO2-P25/(TiO2-P25+TiO2 nanotubes) junction for dye sensitized solar cells. Progress in Natural Science: Materials International. 2016 Aug 1;26(4):375–9.
133. Katoh R, Kasuya M, Kodate S, Furube A, Fuke N, Koide N. Effects of 4-tert-butylpyridine and Li ions on photoinduced electron injection efficiency in black-dye-sensitized nanocrystalline TiO2 films. The Journal of Physical Chemistry C. 2009;113(48):20738–44.
134. Bakr ZH, Wali Q, Ismail J, Elumalai NK, Uddin A, Jose R. Synergistic combination of electronic and electrical properties of SnO2 and TiO2 in a single SnO2-TiO2 composite nanofiber for dye-sensitized solar cells. Electrochim Acta. 2018 Feb 10;263:524–32.

135. Moradi A, Abrari M, Ahmadi M. Efficiency enhancement in dye-sensitized solar cells through the decoration of electro-spun TiO2 nanofibers with Ag nanoparticles. Journal of Materials Science: Materials in Electronics. 2020;31 (19):16759–68.

136. Motlak M, Barakat NAM, Akhtar MS, Hamza AM, Yousef A, Fouad H, et al. Influence of GO incorporation in TiO2 nanofibers on the electrode efficiency in dye-sensitized solar cells. Ceram Int. 2015 Jan 1;41(1):1205–12.

137. Vu HHT, Atabaev TS, Pham-Cong D, Hossain MA, Lee D, Dinh NN, et al. TiO2 nanofiber/nanoparticles composite photoelectrodes with improved light harvesting ability for dye-sensitized solar cells. Electrochim Acta. 2016 Mar 1;193:166–71.

138. Ziyan MAM, Dissanayake M, Zainudeen UL, Senadeera GKR, Thotawatthage CA. Study of dye-sensitized solar cells with TiO2 nanoparticles/nanofibers composite electrode using photovoltic and EIS measurements; 2018.

Peer-review history:
The peer review history for this paper can be accessed here:
https://www.sdiarticle5.com/review-history/119667